

Rayleigh scattering in the transmission spectrum of HAT-P-18b

J. Kirk,^{1*} P. J. Wheatley,^{†1} T. Louden,¹ A. P. Doyle,¹ I. Skillen,² J. McCormac,¹ P. G. J. Irwin,³ and R. Karjalainen²

¹*Department of Physics, University of Warwick, Coventry, CV4 7AL, UK*

²*Isaac Newton Group of Telescopes, Apartado de Correos 321, 38700 Santa Cruz de Palma, Spain*

³*Atmospheric, Oceanic, and Planetary Physics, Clarendon Laboratory, University of Oxford, Parks Road, Oxford OX1 3PU, UK*

Accepted XXX. Received YYY; in original form ZZZ

ABSTRACT

We have performed low-resolution ground-based transmission spectroscopy of the hot Jupiter HAT-P-18b using the ACAM instrument on the William Herschel Telescope (WHT). We detect a bluewards slope extending across our optical transmission spectrum which runs from 4750 Å to 9250 Å. The slope is consistent with Rayleigh scattering at the equilibrium temperature of the planet. We do not detect enhanced sodium absorption, which indicates a high altitude haze is masking the feature and giving rise to the Rayleigh slope. Our detection of an opacity source within a hot Jupiter atmosphere demonstrates that ground-based observations can provide transmission spectra with precision comparable to the Hubble Space Telescope (HST).

Key words: methods: observational -techniques: spectroscopic -planets and satellites: individual: HAT-P-18b -planets and satellites: atmospheres

1 INTRODUCTION

Transmission spectroscopy is an essential tool to characterise the atmospheres of transiting exoplanets (e.g. Charbonneau et al. 2002; Redfield et al. 2008; Snellen et al. 2008). Hot Jupiters lend themselves well to transmission spectroscopy due to their large atmospheric scale heights. The sample of hot Jupiters studied to date is revealing a diverse array of atmospheric chemistries which often depart from clear atmospheres that are predicted to show strong alkali metal absorption and H₂ induced Rayleigh scattering slopes towards the blue optical (Seager & Sasselov 2000; Brown 2001). To date, however, only a single hot Jupiter has been found to display the broad wings of the sodium and potassium features (WASP-39b; Fischer et al. 2016; Sing et al. 2016). Increasingly transmission spectroscopy studies reveal cloud and haze dominated atmospheres that mask the broad wings of sodium and potassium (e.g. Pont et al. 2013; Nikolov et al. 2014) whilst in some cases even the narrow cores are not seen (e.g. Sing et al. 2013). The range of transmission spectra hot Jupiters display was highlighted in a recent survey of 10 hot Jupiters with the Hubble and Spitzer space telescopes (Sing et al. 2016). This

revealed a continuum in hot Jupiter atmospheres from clear atmospheres showing strong alkali metal absorption to cloud and haze dominated atmospheres muting, and sometimes masking entirely, the alkali absorption features.

Ground-based detections of spectral features within hot Jupiter atmospheres have predominantly been of the narrow line cores of sodium (e.g. Zhou & Bayliss 2012; Nikolov et al. 2016) and potassium (e.g. Wilson et al. 2015; Sedaghati et al. 2016). Whilst there have been a couple of detections of bluewards scattering slopes from the ground (e.g. Jordán et al. 2013; Di Gloria et al. 2015), ground based measurements of hot Jupiters have often revealed featureless transmission spectra dominated by clouds (e.g. Kirk et al. 2016; Mallonn et al. 2016). The diversity of these results has emphasised the need to increase the current pool of studied gas giant atmospheres to get a better handle on the processes and parameters governing the presence or absence of clouds and hazes.

In this paper, we present the low-resolution ground-based transmission spectrum of the Saturn-mass planet HAT-P-18b (Hartman et al. 2011). This planet lends itself well to transmission spectroscopy due to the combination of its large atmospheric scale height of 540 km, owing to its low density (0.25 g cm^{-3}), with the small radius of the host ($0.749 R_{\odot}$).

* E-mail: James.Kirk@warwick.ac.uk

† E-mail: P.J.Wheatley@warwick.ac.uk

2 OBSERVATIONS

HAT-P-18 was observed on the night of 2016 April 28th with the ACAM instrument on the 4.2-m William Herschel Telescope, La Palma. ACAM was used in grism spectroscopy mode, which provides low resolution spectroscopy over the entire optical range.

ACAM was used unbinned in fast readout mode with a smaller than standard window to reduce the overhead to ~ 11 seconds with exposure times of 60 seconds. This integration time was used to limit the peak counts of the comparison star to the range of the CCD response characterised as linear. A wide 27 arcsec slit was used to perform these observations to avoid the harmful effects of differential slit losses between the target and its comparison star which can lead to systematics in the derived transmission spectra. To further avoid slit losses, the locations of the spectral traces were monitored throughout the night with manual guiding corrections made to keep the traces within a couple of pixels in the x (spatial) and y (dispersion) directions respectively. A slight defocus was used to maintain the full width at half-maximum (FWHM) at around 1 arcsec. A total of 320 spectra were observed over the course of the night with an airmass varying from $1.93 \rightarrow 1.00 \rightarrow 1.08$ and a moon illumination of 62%. Biases, sky flats and spectra of the CuAr plus CuNe arcs were taken at the start and end of the night.

A comparison star with a similar magnitude to HAT-P-18 was used to perform differential spectroscopy in order to account for telluric variability. The comparison star used was TYC 2594-731-1 at a distance of 3.4 arcmin from HAT-P-18 with a V magnitude of 11.2 and $B-V$ colour of 1.3. HAT-P-18 has a V magnitude of 12.7 and $B-V$ colour of 1.0. The separation between the stars was comfortably within ACAM's slit length of 6.8 arcmin.

3 DATA REDUCTION

To reduce the data, PYTHON scripts were written from scratch to create biases, flat fields and to extract the spectral traces. 51 bias frames were median combined to create a master bias which was subsequently subtracted from each of the science frames. A master flat created from the twilight sky flats was used in an initial reduction. We found that the flat increased the noise in the resulting white light curve and so the master flat was not used in the final reduction. Since the spectral traces are spread across a large number of pixels, the lack of flat fielding did not form a significant source of error.

To extract the spectra, polynomials were fit along each of the two traces in the dispersion direction and fixed apertures placed around these. An iterative polynomial background fit was performed row-by-row across the combined width of the extraction and background apertures and the resulting polynomial subtracted. The iterative nature of this means that the spectral traces themselves are naturally masked from the resulting polynomial which is instead just modelling the background variation in the spatial direction. After subtraction of the polynomial, normal extraction of the counts within the aperture was performed. A number of different extraction and background aperture widths were experimented with to minimise the scatter in the resulting

light curves. This resulted in an optimal aperture width of 30 pixels. The background was calculated from two 50 pixel wide regions, either side of the aperture, at distances of 30 pixels from the edges of the aperture. The pixel scale of ACAM is $0.25 \text{ arcsec pixel}^{-1}$. The errors in the data points were a combination of the photon noise and the readnoise of ACAM which in fast readout mode is $7 \text{ electrons pixel}^{-1}$ with a gain of $1.9 \text{ electrons count}^{-1}$.

After extraction of the spectral traces, cosmic rays were removed. This was done by first dividing each spectral frame by a reference frame clean of cosmics. This self-division of each spectral trace resulted in spikes where cosmic rays were located. The flux values of the pixels affected by cosmic rays were then replaced by interpolating between the two nearest neighbouring pixels unaffected by the cosmic ray.

Due to the rotation of the trace on the CCD throughout the night, resulting from instrumental and astrophysical affects, the spectra were aligned in wavelength so that accurate differential spectroscopy could be performed. This was done by cross-correlating regions of each spectral frame with a reference frame around significant absorption features. This was done across the spectrum and allowed for the shift relative to the reference to be calculated as a function of location on the chip. A third order polynomial was then fitted to these shifts and the individual spectra resampled onto the grid of the reference spectrum. The shifts for each star's spectra were calculated individually before resampling onto the same grid. This resulted in the spectra of both stars being well aligned for all frames.

With the spectra aligned in pixel space, the wavelength solution was calculated using strong telluric and stellar absorption lines. A synthetic spectrum of telluric and spectral lines with a resolution of $R = 1000$ was generated for a star of the same temperature, surface gravity and metallicity as HAT-P-18 which was cross-correlated with the observed spectrum. This gave the wavelength as a function of pixel position for a number of strong features. A second-order polynomial was then fitted to convert from pixel position into wavelength. Since arcs were only taken through a 1 arcsec slit at the beginning and end of the night, to reduce the time spent off target, the arcs were only used as a cross check to the solution found through the stellar and telluric lines.

For further analysis the very blue and very red ends of the spectra were excluded due to low signal to noise and differential vignetting between the target and comparison. This resulted in the spectra spanning a wavelength range between 4750 \AA and 9250 \AA .

4 DATA ANALYSIS

4.1 Light curve fitting

With the data reduced and spectra extracted, we binned the data into 250 \AA -wide wavelength bins running from 4750 \AA to 9250 \AA . The bin containing the strong telluric oxygen feature at $\sim 7600 \text{ \AA}$ showed a significant level of red noise and so this bin was masked from further analysis. This resulted in seventeen 250 \AA -wide bins. The bin locations are shown in Fig. 1 with the masked region shaded grey.

We fitted the light curves with analytic transit light curves using a quadratic limb darkening law

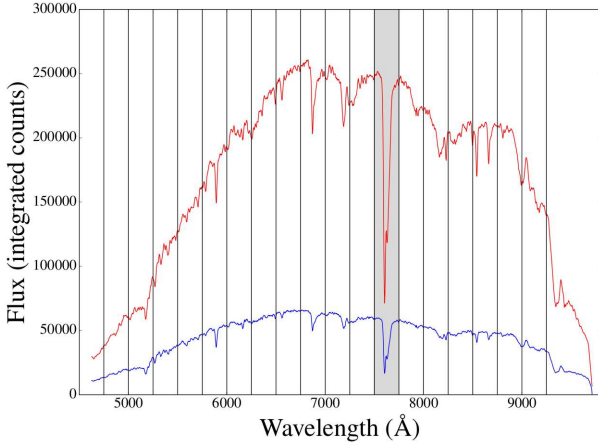


Figure 1. Locations of the seventeen 250 Å-wide bins used in the wavelength bin fitting. The target’s spectrum is shown in blue and the comparison’s in red. The grey region shows the bin containing the strong telluric feature that was excluded from further analysis.

(Mandel & Agol 2002). A long time-scale trend was simultaneously fitted to model the overall trend. We experimented with different functions to fit this trend, which were: a quadratic in time polynomial, a cubic in time polynomial, a linear in time extinction coefficient and a quadratic in time extinction coefficient. Whilst all functions resulted in transmission spectra with blueward slopes, the cubic in time polynomial was adopted due to the better Bayesian Information Criterion (BIC; Schwarz et al. 1978). The parameters defining the model were: the radius ratio of planet to star R_P/R_* , the scaled stellar radius a/R_* , the inclination i , the quadratic limb darkening coefficients u_1 and u_2 , the time of mid-transit T_c , and the four parameters defining the long time-scale trend.

The light curve models were initially fitted using SCIPY’s OPTIMIZE package within PYTHON (Jones et al. 2001) using a Nelder-Mead algorithm to perform the minimisation (Nelder & Mead 1965). With the results from this fit a Markov chain Monte Carlo (MCMC) was initiated at these values and was implemented using the PYTHON package EMCEE (Foreman-Mackey et al. 2013).

The system parameters (a/R_* , i and T_c) were held fixed to the results from a fit to the white light curve (Table 2). This was created simply by summing the seventeen individual wavelength binned light curves. We did this as we are interested in the relative error in the planetary radius between wavelengths and not in the absolute error in the radius. By fixing these system parameters shared between the wavelength bins, we remove them as sources of error within the relative radii.

We experimented with our treatment of the limb darkening by having both coefficients as fit parameters, with no priors, and having one coefficient fixed and the other as a fit parameter. When we chose to fix one of the coefficients, we made use of the limb darkening toolkit (LDTK, Parviainen & Aigrain 2015) which uses PHOENIX models (Husser et al. 2013) to calculate u_1 and u_2 with errors propagated from the errors in the stellar parameters. In all cases, we found that the limb darkening coefficients were well constrained and the resulting values were consistent whether

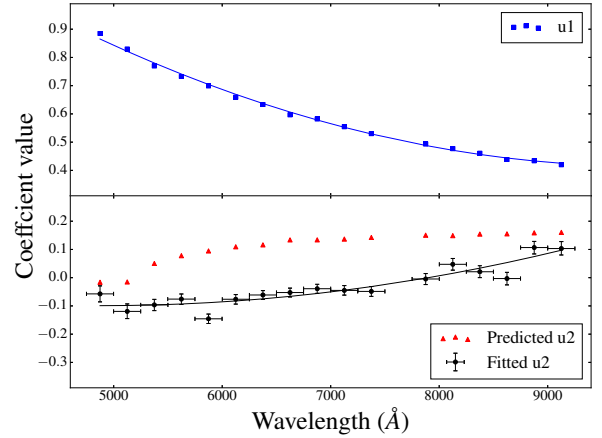


Figure 2. Top panel: the LDTK generated values for the first limb darkening coefficient u_1 (blue squares) with the function used to describe these in all the wavelength binned light curve fits (solid blue line). Bottom panel: the fitted values for the second limb darkening coefficient u_2 following the first run of the MCMC (black error bars) with the function used to describe these in the second run of the MCMC (black line). The predicted values for u_2 generated by LDTK are shown by the red triangles.

one or both were fitted parameters. It is well known that the quadratic limb darkening coefficients are degenerate (e.g. Southworth 2008) and often one coefficient is held fixed whilst the other is fitted for (e.g. Kirk et al. 2016). As mentioned above, we are interested in the relative radii in the error and so fixing one of the limb darkening coefficients removes this as a source of error within R_P/R_* . We found that the overall shape of the transmission spectra did not change whether we fitted for one or both limb darkening coefficients. Since each limb darkening coefficient can be described by a smoothly varying function of wavelength we decided to incorporate this within our light curve model.

When fixing one limb darkening parameter we first fitted a second order polynomial to the expected values of u_1 from LDTK as a function of wavelength (Fig. 2, top panel). This function was then used to describe u_1 in the subsequent light curve fits, removing u_1 as a fit parameter. This left R_P/R_* , u_2 , and the four parameters defining the long time-scale trend as fit parameters. We placed a uniform prior on u_2 such that $(u_1 + u_2) \leq 1$ and placed no priors on the other parameters. With the starting values resulting from the Nelder-Mead minimisation, an initial MCMC to each wavelength binned light curve was run for 1000 iterations with 120 walkers ($20 \times n_p$, where n_p is the number of parameters). The first 500 steps were discarded as the chains were burning-in. The best fitting model resulting from this initial run was then used to rescale the error bars giving $\chi^2_\nu = 1$ for each wavelength bin.

Following the initial run of the MCMC, we fitted a second order polynomial to the resulting values for u_2 to describe u_2 as a function of wavelength (Fig. 2, bottom panel). A second MCMC was then run with 100 walkers ($20 \times n_p$) for 1000 steps with this function describing u_2 , thus removing it as fit parameter. The lower panel of Fig. 2 shows the function (black line) fitted to the derived values of u_2 (black error bars) compared to the predicted values of u_2 from LDTK (red triangles).

Table 1. Results from the fitting of the wavelength binned light curves shown in Fig. 3.

Bin	R_P/R_*	$u1$	$u2$
4750 – 4999 Å	$0.14114^{+0.00082}_{-0.00086}$	0.87	−0.099
5000 – 5249 Å	$0.13899^{+0.00065}_{-0.00067}$	0.82	−0.099
5250 – 5499 Å	0.13996 ± 0.00056	0.78	−0.097
5500 – 5749 Å	0.13964 ± 0.00047	0.74	−0.093
5750 – 5999 Å	$0.13958^{+0.00042}_{-0.00043}$	0.70	−0.089
6000 – 6249 Å	$0.13821^{+0.00044}_{-0.00043}$	0.67	−0.082
6250 – 6499 Å	$0.13879^{+0.00046}_{-0.00043}$	0.64	−0.075
6500 – 6749 Å	$0.13908^{+0.00045}_{-0.00043}$	0.61	−0.066
6750 – 6999 Å	$0.13870^{+0.00048}_{-0.00045}$	0.58	−0.056
7000 – 7249 Å	$0.13804^{+0.00040}_{-0.00041}$	0.55	−0.044
7250 – 7499 Å	$0.13851^{+0.00047}_{-0.00046}$	0.53	−0.032
7750 – 7999 Å	$0.13679^{+0.00045}_{-0.00047}$	0.49	−0.002
8000 – 8249 Å	$0.13782^{+0.00048}_{-0.00050}$	0.47	0.015
8250 – 8499 Å	0.13854 ± 0.00050	0.46	0.034
8500 – 8749 Å	$0.13793^{+0.00077}_{-0.00078}$	0.44	0.053
8750 – 8999 Å	$0.13757^{+0.00055}_{-0.00056}$	0.43	0.075
9000 – 9249 Å	$0.13719^{+0.00061}_{-0.00064}$	0.43	0.097

The fitted models to the wavelength bins are shown in Fig. 3 with the results in Table 1.

4.2 Transmission spectrum

Following the fitting of the wavelength binned light curves, we constructed the resulting transmission spectrum which is displayed in Fig. 4. This revealed a strong blueward slope across the transmission spectrum, resembling a Rayleigh scattering signature.

Rayleigh scattering has been seen in a number of planets to date by HST (e.g. Pont et al. 2013; Fischer et al. 2016) and a couple from the ground (Jordán et al. 2013; Di Gloria et al. 2015).

A Rayleigh scattering slope is plotted on this figure at the equilibrium temperature of the planet (852 K; Hartman et al. 2011), with a slope given by Lecavelier Des Etangs et al. (2008) as

$$\frac{dR_p}{d \ln \lambda} = \frac{k}{\mu g} \alpha T \quad (1)$$

where μ is the mean molecular mass of an atmospheric particle taken to be 2.3 times the mass of a proton, k is the Boltzmann constant, g is the planet's surface gravity, $\alpha = -4$ as expected for Rayleigh scattering, and T we take as the equilibrium temperature.

The transmission spectrum of HAT-P-18b is well fitted by a Rayleigh slope at the equilibrium temperature of the planet (Fig. 4), with a $\chi^2_\nu = 1.2$.

We also plot on Fig. 4 a clear atmosphere model (in blue) as resulting from the NEMESIS radiative transfer code (Irwin et al. 2008), binned to the resolution of the data. The clear atmosphere model does not provide as good a fit as the Rayleigh scattering slope, as we do not detect the broad wings of the strong sodium and potassium features. This indicates a condensate haze is masking the wings as in e.g. HD 189733b (Pont et al. 2008; Sing et al. 2011;

Pont et al. 2013), WASP-31b (Sing et al. 2015) and WASP-6b (Jordán et al. 2013; Nikolov et al. 2015).

4.3 Targeted sodium search

While clouds and hazes can mask the broad wings of sodium, it is possible for the narrow line core, that arises from high altitudes, to still be visible. We performed a separate targeted search for the narrow feature of sodium using eight 50 Å-wide bins running from 5670 – 6070 Å, with one bin centred on the sodium doublet. This revealed significant red noise in the bin containing the Na feature, which can be seen in Fig. 5, and could either be telluric or stellar in nature. To properly account for this red noise, and to obtain robust errors for the transit depth, we used a Gaussian Process (GP).

The GP was implemented through the GEORGE PYTHON package (Ambikasaran et al. 2014). The mean function of the GP in each wavelength bin was the quadratically limb-darkened analytic transit light curve (Mandel & Agol 2002). We treated the limb darkening in the same way as described in section 4.1. We used a Matérn 3/2 kernel to model correlations in the data, defined by the hyper-parameters τ (the time-scale) and a (the amplitude), in addition to a white-noise kernel defined by the variance σ . The fit parameters were therefore R_P/R_* , $u2$, a , τ and σ . We used loose, uniform priors to encourage convergence.

An initial MCMC was run for 2000 steps with 100 walkers ($20 \times n_p$) with the first 1000 steps discarded as burn-in. Similar to the 250 Å-wide wavelength binned light curve fits, we then ran a second MCMC with a function describing the fitted values of $u2$ resulting from the first run, thus removing $u2$ as a fit parameter. The second run was 2000 steps long with 80 walkers ($20 \times n_p$).

The wavelength binned fits with the GP are shown in Fig. 5, which displays the power of the GP to model the red noise in bin 5 whilst not overfitting the data. The transmission spectrum around the sodium feature is shown in Fig. 6, which shows we do not detect sodium in the atmosphere at a resolution of 50 Å.

Whilst we attempted a targeted potassium search, unfortunately due to the potassium line's proximity to the strong telluric feature, we were unable to place constraints on the presence of this.

4.4 GP fit to all wavelength bins

Whilst the model described in section 4.1 provided good fits to the data (Fig. 3), we wanted to confirm that these results were independent of the function used to model the long time-scale trend. To do this, we again used a Gaussian Process, with the same kernel as used in section 4.3 but this time applied to the seventeen 250 Å-wide bins and with system parameters held fixed to a fit to the white light curve with a GP (Table 2). The transmission spectrum resulting from these fits is shown in Fig. 7. This test confirmed the blueward slope seen in Fig. 4 was independent of the choice of system parameters derived with and without GPs and also independent of the function used to model the long time-scale trend. Fig. 7 reveals a transmission spectrum which is again consistent with a Rayleigh scattering slope at the equilibrium temperature of the planet. In this case the

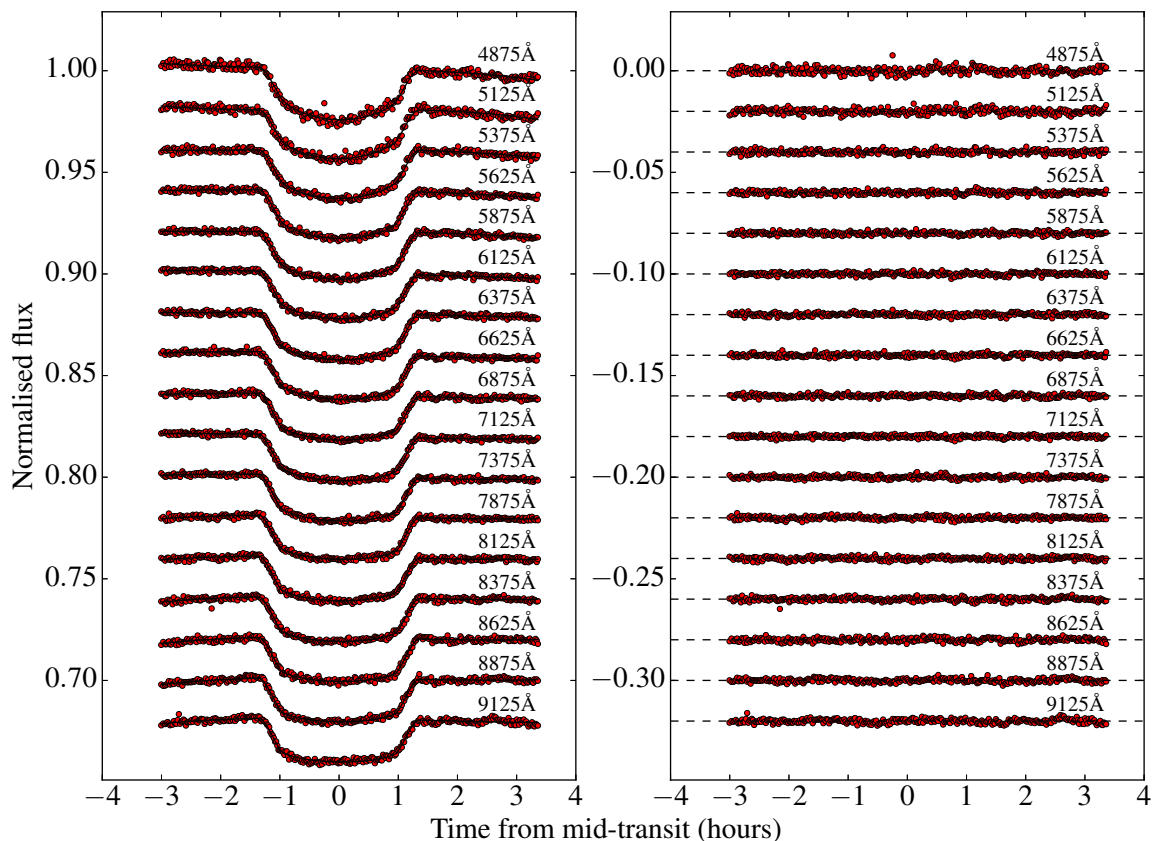


Figure 3. Left-hand panel: Our fits to the wavelength binned light curves of HAT-P-18b, going from blue (top) to red (bottom). Right-hand panel: the residuals to the fits in the left-hand panel after subtracting the best fitting model.

transmission spectrum is also more consistent with the clear atmosphere model (blue line, Fig. 6) than the transmission spectrum obtained without the use of GPs (Fig. 4). However, given that we do not detect sodium, the transmission spectrum cannot be explained by a clear atmosphere.

4.5 Unocculted spots

Although we do not observe any occultations of star spots within the transit of HAT-P-18b, we do need to take into account the possibility of star spots that may be present on the surface of the star but are not along the transit chord. Seeliger et al. (2015) monitored the activity of HAT-P-18 over a timespan of 12 months. They found a mean variation in the R -band brightness of HAT-P-18 of only ~ 0.9 mmag which they find is consistent with no variation when taking their error bars into account. Therefore HAT-P-18 does not show strong activity induced photometric variation and so we do not expect unocculted activity regions to have a noticeable effect on the transmission spectrum. Nevertheless, we quantify their effects below.

Unocculted spots and plagues can have the effect of inducing a slope mimicking Rayleigh scattering within the transmission spectrum and so their effect needs to be considered (McCullough et al. 2014; Oshagh et al. 2014). These unocculted spots can be accounted for by a wavelength dependent depth correction. As with Kirk et al. (2016) we fol-

low the formalism of Sing et al. (2011) to make this correction.

We use ATLAS9 stellar models (Kurucz 1993) of a star with a temperature of 4750 K and spot temperatures with a temperature difference ΔT ranging from 250 – 1250 K. Using this variation we assume a total dimming of 0.1 % at a reference wavelength of 6000 Å and use equations 4 and 5 of Sing et al. (2011) to find the correction in R_P/R_* across a wavelength range spanning 4500 – 9500 Å. The result of this is shown in Fig. 8, where the effect of spots on this star is minimal.

Berdyugina (2005) fitted a function to observed spot temperature contrasts for a number of stellar types. For K2 dwarfs, like HAT-P-18, the predicted ΔT is ≈ 1250 K. Taking this ΔT and the correction in Fig. 8 we propagate this through to the transmission spectrum (Fig. 9). This correction is very small and within the 1σ errors and thus unocculted spots cannot be the cause of the blueward slope seen in the transmission spectrum.

4.6 Updated system parameters

With the high quality light curves we were able to compare the results from our white light curve fitting to those published in the literature (Table 2). Whilst our results are consistent with previous studies, we improve the precision in these parameters.

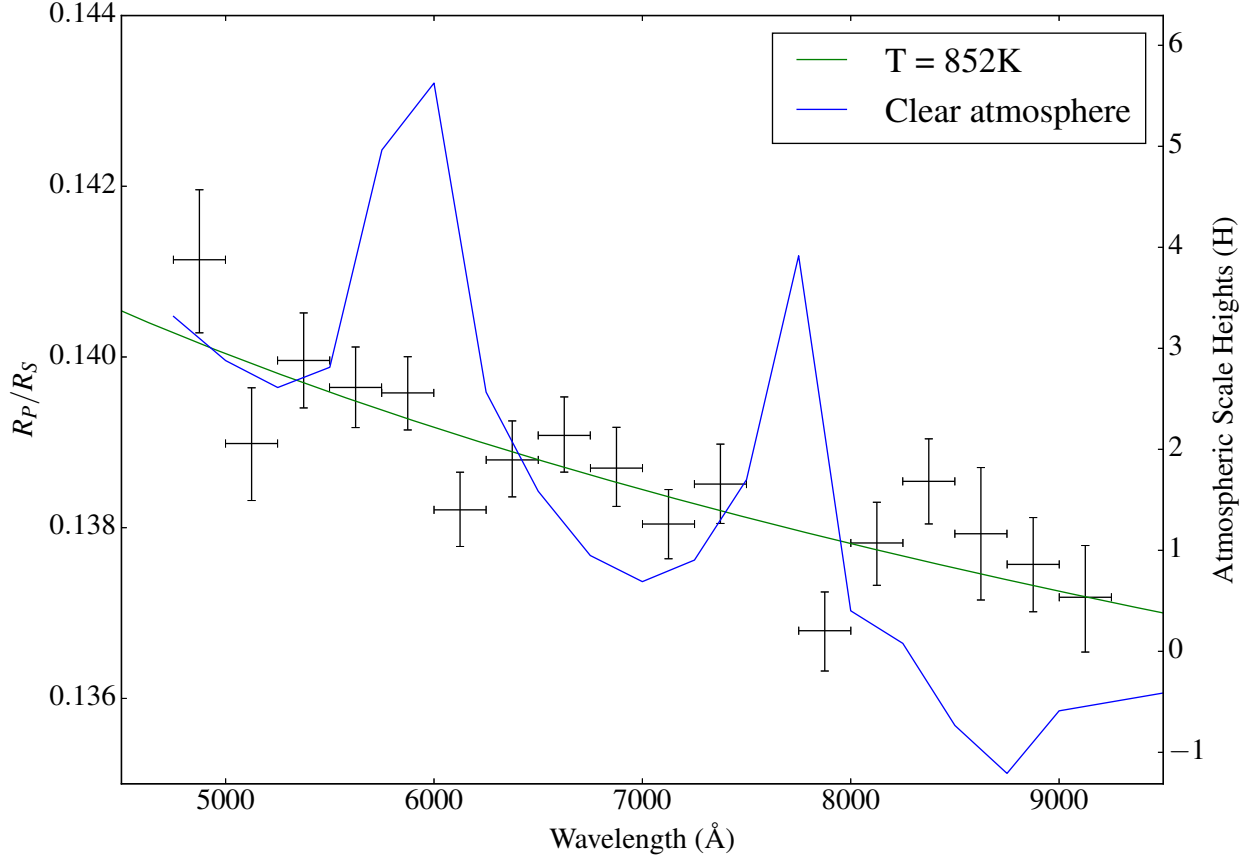


Figure 4. Transmission spectrum of HAT-P-18b with a Rayleigh scattering slope at the equilibrium temperature of the planet (852 K) plotted in green. The blue line shows a clear atmosphere model, binned to the size of the data points, highlighting the absence of the broad wings of the Na and K features, indicating the presence of a high altitude haze.

Table 2. Comparison of system parameters to previous studies, resulting from the fits of a cubic in time polynomial and a Gaussian Process to the white light curve. Although these values are consistent, the GP fit produces slightly larger errors, as expected, and so should be adopted as our conservative final values.

Parameter	This work	Seeliger et al. (2015)	Esposito et al. (2014)	Hartman et al. (2011)
<i>Cubic polynomial</i>				
R_P/R_*	$0.1385^{+0.0010}_{-0.0011}$	0.1362 ± 0.0011	0.136 ± 0.011	0.1365 ± 0.0015
i (deg.)	$88.63^{+0.12}_{-0.10}$	88.79 ± 0.21	88.79 ± 0.25	88.8 ± 0.3
a/R_*	$16.71^{+0.18}_{-0.16}$	17.09 ± 0.71	16.76 ± 0.82	16.04 ± 0.75
T_c (BJD, days)	$2457507.59300891 \pm 0.000060$	$2454715.02254 \pm 0.00039$	2455706.7 ± 0.7	$2454715.02174 \pm 0.00020$
<i>Gaussian Process</i>				
R_P/R_*	$0.1356^{+0.0028}_{-0.0024}$	0.1362 ± 0.0011	0.136 ± 0.011	0.1365 ± 0.0015
i (deg.)	$88.53^{+0.16}_{-0.13}$	88.79 ± 0.21	88.79 ± 0.25	88.8 ± 0.3
a/R_*	$16.39^{+0.24}_{-0.23}$	17.09 ± 0.71	16.76 ± 0.82	16.04 ± 0.75
T_c (BJD, days)	$2457507.59219566^{+0.000194}_{-0.000181}$	$2454715.02254 \pm 0.00039$	2455706.7 ± 0.7	$2454715.02174 \pm 0.00020$

5 DISCUSSION

The transmission spectrum of HAT-P-18b displays a gradient rising towards the blue (Fig. 4), which is consistent with Rayleigh scattering at the equilibrium temperature of the planet (852 K). Whilst we detect the Rayleigh slope, we do not detect either the broad wings of sodium or the line core in a 50 Å-wide bin (Fig. 6). This suggests that a high altitude haze is masking the sodium feature in the atmo-

sphere and giving rise to the Rayleigh slope, similar to e.g. WASP-12b (Sing et al. 2013), WASP-6b (Jordán et al. 2013; Nikolov et al. 2014) and HAT-P-12b (Sing et al. 2016). A haze is also preferable due to the poor fit of the clear atmosphere model in Fig. 4.

HAT-P-18b with an equilibrium temperature of 852 K (Hartman et al. 2011) is cooler than any of the planets studied by Sing et al. (2016) in their recent survey of 10

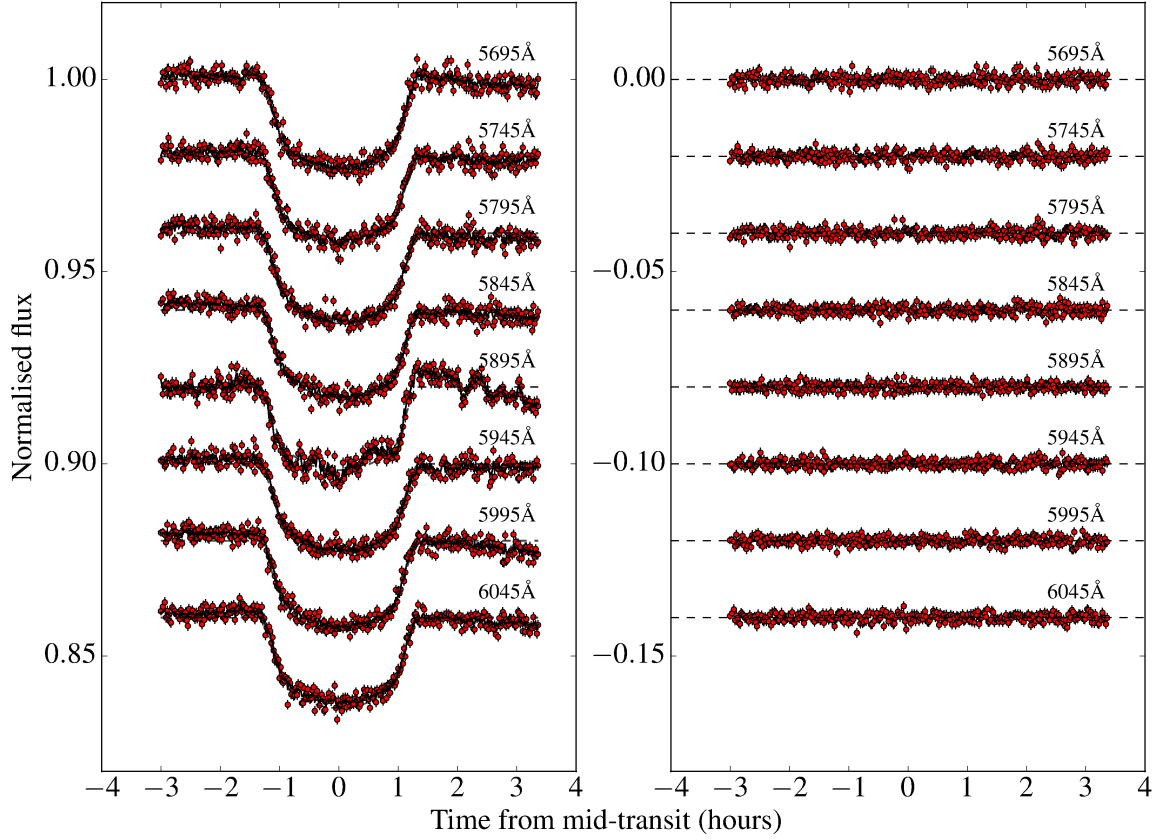


Figure 5. Left-hand panel: fits to the 50 Å-wide wavelength bins around the sodium feature. We use a Gaussian Process to model these light curves due to the significant correlated noise visible at 5895Å. The dashed lines indicate the underlying Mandel & Agol (2002) transit model defining the mean function of the GP. Right-hand panel: the residuals to the fits in the left-hand panel after subtracting the best fitting model.

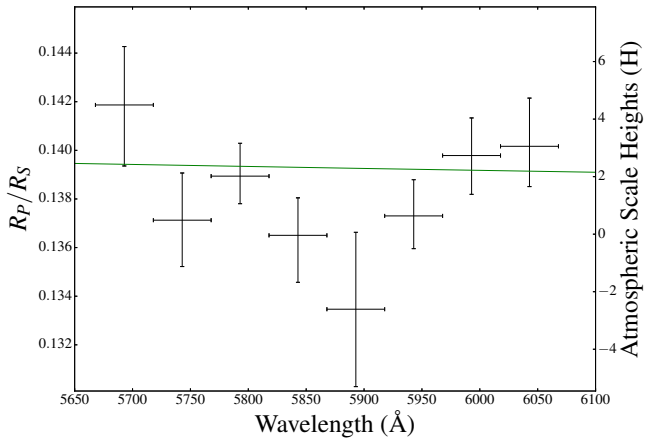


Figure 6. The transmission spectrum centred around the sodium feature at a resolution of 50 Å, which is not detected. The green line indicates a Rayleigh slope at the equilibrium temperature of the planet.

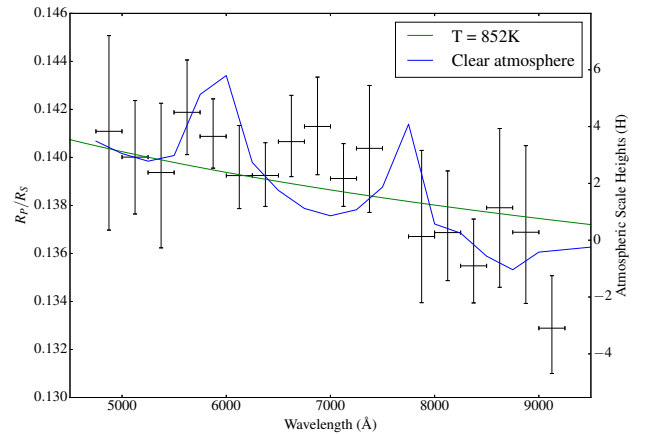


Figure 7. Full transmission spectrum resulting from the use of Gaussian Processes, indicating an atmosphere consistent with Rayleigh scattering at the equilibrium temperature of the planet (green line). The lack of the sodium core indicates that the transmission spectrum is inconsistent with a clear atmosphere model at this resolution (blue line).

hot Jupiters. The nearest comparison object is HAT-P-12b (Hartman et al. 2009) with an equilibrium temperature of 963 K. For this object, Sing et al. (2016) found a haze layer leading to a strong Rayleigh scattering slope extend-

ing across the optical spectrum and also detected potassium absorption although did not detect sodium. Whilst this might indicate some correlation of haze with temperature, Sing et al. (2016) found that the presence of clouds

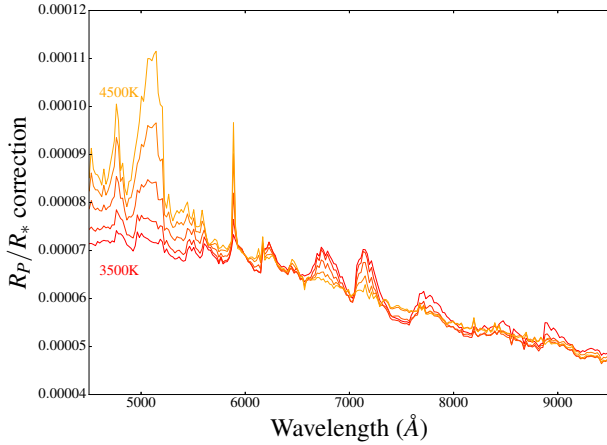


Figure 8. Correction in R_P/R_* due to the affect of unocculted spots with temperatures ranging from 3500 K (red) to 4500 K (orange) leading to a total dimming of the star of 0.1% (Seeliger et al. 2015).

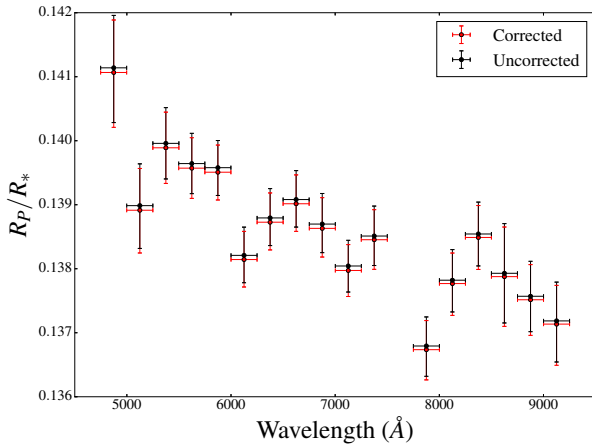


Figure 9. Correction in the transmission spectrum due to unocculted spots assuming a spot with $\Delta T = 1250$ K, appropriate for K2 dwarfs (Berdyugina 2005). The uncorrected points are in black and the corrected are in red. This highlights the negligible depth correction due to unocculted spots in the case of HAT-P-18.

and hazes is not strongly dependent on temperature in their sample.

The difficulty in pinning down the relation between the presence of clouds and hazes and the planetary parameters was further highlighted in the discussion of Fischer et al. (2016) concerning the clear atmosphere of WASP-39b, which is the only hot Jupiter studied to date in which the broad wings of both sodium and potassium are visible. In this paper the authors consider, among other parameters, the role of surface gravity and metallicity on the planet's atmosphere. If surface gravity were the dominant factor, leading to differences in the settling rates of condensates, we would expect to see condensates in the atmosphere of WASP-39b also as it has a lower surface gravity ($\log g = 2.61$, Faedi et al. 2011) than both HAT-P-12b ($\log g = 2.75$, Hartman et al. 2009) and HAT-P-18b ($\log g = 2.69$, Hartman et al. 2011), which is not seen in the data. If we consider metallicity, HAT-P-18 has a higher [Fe/H] ratio of

0.1 than both HAT-P-12 (-0.29) and WASP-39 (-0.12). Taking the stellar metallicity as a proxy for the planet metallicity, the higher metallicity of HAT-P-18b might be related to the presence of condensates in its atmosphere, whilst the absence of these in the atmosphere of WASP-39b could be related to its lower metallicity. This argument however breaks down when considering HAT-P-12b which has a metal-poor host yet a condensate haze layer. It seems the presence of a haze layer is therefore not simply determined by a single parameter.

6 CONCLUSIONS

We have studied the transmission spectrum of the hot Jupiter HAT-P-18b using the low-resolution grism spectrograph ACAM on the William Herschel Telescope. We find a strong blueward scattering slope, extending across our transmission spectrum from 4750 – 9250 Å, consistent with Rayleigh scattering at the equilibrium temperature of the planet. We do not detect enhanced absorption around the sodium doublet, suggesting a high altitude haze is masking this feature whilst giving rise to the Rayleigh slope. We consider the effect of unocculted spots and find that the slope cannot be explained by these. This is only the third detection of a scattering slope from the ground.

We do not try to place constraints on the presence of potassium due to the strong neighbouring telluric features but do improve the precision in the system parameters with our very high precision light curves.

This work demonstrates the role that ground based transmission spectroscopy can play in the detection of atmospheric opacity sources with precision comparable to HST.

ACKNOWLEDGEMENTS

J.K. is supported by a Science and Technology Facilities Council (STFC) studentship. P.W. is supported by an STFC consolidated grant (ST/L00073). This work made use of the ASTROPY (Astropy Collaboration et al. 2013), NUMPY (Van Der Walt et al. 2011) and MATPLOTLIB (Hunter 2007) PYTHON packages in addition to those cited within the body of the paper. The William Herschel Telescope is operated on the island of La Palma by the Isaac Newton Group in the Spanish Observatorio del Roque de los Muchachos of the Instituto de Astrofísica de Canarias. The ACAM spectroscopy was obtained as part of W/2016A/32.

REFERENCES

- Ambikasaran S., Foreman-Mackey D., Greengard L., Hogg D. W., O’Neil M., 2014, preprint, ([arXiv:1403.6015](https://arxiv.org/abs/1403.6015))
- Astropy Collaboration et al., 2013, *A&A*, **558**, A33
- Berdyugina S. V., 2005, *LRSP*, **2**, 8
- Brown T. M., 2001, *ApJ*, **553**, 1006
- Charbonneau D., Brown T. M., Noyes R. W., Gilliland R. L., 2002, *ApJ*, **568**, 377
- Di Gloria E., Snellen I., Albrecht S., 2015, *A&A*, **580**, A84
- Esposito M., et al., 2014, *A&A*, **564**, L13
- Faedi F., et al., 2011, *A&A*, **531**, A40
- Fischer P. D., et al., 2016, *ApJ*, **827**, 19

- Foreman-Mackey D., Hogg D. W., Lang D., Goodman J., 2013, *PASP*, 125, 306
- Hartman J. D., et al., 2009, *ApJ*, 706, 785
- Hartman J. D., et al., 2011, *ApJ*, 726, 52
- Hunter J. D., 2007, *Computing In Science & Engineering*, 9, 90
- Husser T.-O., Wende-von Berg S., Dreizler S., Homeier D., Reiners A., Barman T., Hauschildt P. H., 2013, *A&A*, 553, A6
- Irwin P., et al., 2008, *Journal of Quantitative Spectroscopy and Radiative Transfer*, 109, 1136
- Jones E., Oliphant T., Peterson P., et al., 2001, SciPy: Open source scientific tools for Python, <http://www.scipy.org/>
- Jordán A., et al., 2013, *ApJ*, 778, 184
- Kirk J., Wheatley P. J., Loudon T., Littlefair S. P., Copperwheat C. M., Armstrong D. J., Marsh T. R., Dhillon V. S., 2016, *MNRAS*, 463, 2922
- Kurucz R., 1993, ATLAS9 Stellar Atmosphere Programs and 2 km/s grid. Kurucz CD-ROM No. 13. Cambridge, Mass.: Smithsonian Astrophysical Observatory, 1993., 13
- Lecavelier Des Etangs A., Pont F., Vidal-Madjar A., Sing D., 2008, *A&A*, 481, L83
- Mallonn M., et al., 2016, *MNRAS*, 463, 604
- Mandel K., Agol E., 2002, *ApJ*, 580, L171
- McCullough P., Crouzet N., Deming D., Madhusudhan N., 2014, *ApJ*, 791, 55
- Nelder J. A., Mead R., 1965, *The computer journal*, 7, 308
- Nikolov N., et al., 2014, *MNRAS*, 437, 46
- Nikolov N., et al., 2015, *MNRAS*, 447, 463
- Nikolov N., Sing D. K., Gibson N. P., Fortney J. J., Evans T. M., Barstow J. K., Kataria T., Wilson P. A., 2016, preprint, ([arXiv:1610.01186](https://arxiv.org/abs/1610.01186))
- Oshagh M., Santos N., Ehrenreich D., Haghighipour N., Figueira P., Santerne A., Montalto M., 2014, *A&A*, 568, A99
- Parviainen H., Aigrain S., 2015, *MNRAS*, 453, 3821
- Pont F., Knutson H., Gilliland R. L., Moutou C., Charbonneau D., 2008, *MNRAS*, 385, 109
- Pont F., Sing D. K., Gibson N. P., Aigrain S., Henry G., Husnoo N., 2013, *MNRAS*, 432, 2917
- Redfield S., Endl M., Cochran W. D., Koesterke L., 2008, *ApJ*, 673, L87
- Schwarz G., et al., 1978, *The annals of statistics*, 6, 461
- Seager S., Sasselov D. D., 2000, *ApJ*, 537, 916
- Sedaghati E., et al., 2016, preprint, ([arXiv:1609.03906](https://arxiv.org/abs/1609.03906))
- Seeliger M., et al., 2015, *MNRAS*, 451, 4060
- Sing D. K., et al., 2011, *MNRAS*, 416, 1443
- Sing D. K., et al., 2013, *MNRAS*, 436, 2956
- Sing D. K., et al., 2015, *MNRAS*, 446, 2428
- Sing D. K., et al., 2016, *Nature*, 529, 59
- Snellen I. A. G., Albrecht S., de Mooij E. J. W., Le Poole R. S., 2008, *A&A*, 487, 357
- Southworth J., 2008, *MNRAS*, 386, 1644
- Van Der Walt S., Colbert S. C., Varoquaux G., 2011, *Computing in Science & Engineering*, 13, 22
- Wilson P. A., et al., 2015, *MNRAS*, 450, 192
- Zhou G., Bayliss D. D. R., 2012, *MNRAS*, 426, 2483

This paper has been typeset from a \LaTeX file prepared by the author.